



## Zonal circulation in the North Atlantic ocean at 52°W from WOCE-WHP and CLIVAR sections: 1997, 2003 and 2012

Daniel Santana-Toscano<sup>a,\*</sup>, M. Dolores Pérez-Hernández<sup>a</sup>, Alison M. Macdonald<sup>b</sup>,  
Cristina Arumí-Planas<sup>a</sup>, Verónica Caínzos<sup>a</sup>, Alonso Hernández-Guerra<sup>a</sup>

<sup>a</sup> Unidad Océano y Clima, Instituto de Oceanografía y Cambio Global, IOCAG, Universidad de Las Palmas de Gran Canaria, ULPGC, Unidad Asociada ULPGC-CSIC, Canary Islands, Spain

<sup>b</sup> Woods Hole Oceanographic Institution, Woods Hole, MA, USA

### ARTICLE INFO

#### Keywords:

Western Subtropical Gyre  
Inverse box model  
Western Boundary Currents

### ABSTRACT

The A20 line is a meridional hydrographic section located at 52°W that cuts through the western North Atlantic Subtropical Gyre (NASG). It encloses the main paths of the Atlantic Meridional Overturning Circulation (AMOC). Using data from three A20 hydrographic cruises carried out in 1997, 2003 and 2012 together with Acoustic Doppler Current Profiler data and the velocities from an inverse box model, the circulation of the western NASG is estimated. The Gulf Stream is the main poleward path of the AMOC, carrying  $155.3 \pm 11.1$ ,  $102.7 \pm 13.5$  and  $181.1 \pm 14.9$  Sv in 1997, 2003 and 2012, respectively ( $1 \text{ Sv} = 10^6 \text{ m}^3/\text{s} \sim 10^9 \text{ kg/s}$ ). In opposite direction, the Deep Western Boundary Current crosses the section at the northern/southern boundaries with a mass transport of  $-21.2 \pm 8.9/29.0 \pm 9.1$ ,  $-14.4 \pm 10.8/14.2 \pm 8.1$  and  $-37.9 \pm 10.2/44.5 \pm 9.8$  Sv in 1997, 2003 and 2012, respectively. A net heat exchange from the ocean to the atmosphere is estimated to be  $-0.7 \pm 0.1$  PW and  $-0.6 \pm 0.1$  PW in 1997 and 2012, respectively, but is negligible in 2003 ( $0.1 \pm 0.1$  PW). The freshwater flux is significantly lower in 2003 ( $0.3 \pm 0.1$  Sv) than in 1997 ( $0.6 \pm 0.1$  Sv) and 2012 ( $0.6 \pm 0.1$  Sv). Ocean numerical models such as ECCO, GLORYS and MOM are used to address the interannual variability between the three surveys, but only the GLORYS output roughly agrees with the hydrographic data. GLORYS suggests a heat transport from the ocean to the atmosphere throughout the year and a net freshwater flux supported by precipitation plus river runoff higher than evaporation in all seasons except the spring.

### 1. Introduction

From 1990 to 2002 the World Ocean Circulation Experiment Hydrographic Program (WOCE-WHP) collected and analyzed hydrographic data across the globe. This experiment set the basis for the later Climate Variability Hydrographic Program (CLIVAR). All international, WOCE-WHP and CLIVAR have globally organized ship-based hydrographic surveys and have established standard sections that have allowed interannual comparisons. In addition, by creating an open-access database, they have merged the effort of individual countries and have given visibility to single surveys.

The meridional A20 section is located along 52°W, in the western North Atlantic Subtropical Gyre (NASG), where the main currents of the Atlantic Meridional Overturning Circulation (AMOC) are present (Fig. 1). It was firstly sampled in summer of 1997, and, later, in fall of 2003 and spring of 2012. The western basin of the NASG is the main

route for the warm poleward waters that feed the upper limb of the AMOC. The Gulf Stream (GS) is the main current flowing towards higher latitudes along the North American slope. The GS splits into two branches, the weaker branch recirculates to the eastern Subtropical Gyre and the stronger one flows northward to high latitudes (Pérez-Hernández et al., 2013; Vélez-Belchí et al., 2017; Worthington, 1976). This stronger branch exchanges heat with the atmosphere and becomes colder, denser and, therefore, sinks into deep layers of the ocean forming the Deep Western Boundary Current (DWBC; Pérez-Hernández et al., 2019; Reid, 1994; Våge et al., 2013; Casanova-Masjoan et al., 2020; Schott et al., 2004). The DWBC forms the lower limb of the AMOC and is the main southward flow carrying dense cold water formed at high latitudes through the western NASG Gyre (Bower et al., 2019; Munk, 1950; Reid, 1994; Schott et al., 2004; Stommel et al., 1958; Stommel, 1948).

In this work, the main goal was to quantify the circulation pattern in

\* Corresponding author.

E-mail address: [daniel.santana@ulpgc.es](mailto:daniel.santana@ulpgc.es) (D. Santana-Toscano).

<https://doi.org/10.1016/j.pocean.2023.103069>

Received 9 January 2023; Received in revised form 7 June 2023; Accepted 12 June 2023

Available online 17 June 2023

0079-6611/© 2023 The Author(s). Published by Elsevier Ltd. This is an open access article under the CC BY license (<http://creativecommons.org/licenses/by/4.0/>).

the western boundary of the NASG and to estimate the changes in the main components of the AMOC using the three A20 hydrographic sections carried out in 1997, 2003 and 2012. These results are compared with output from climatology-forced and free-running models to determine which had better agreement with the results from in-situ observations. Heat and freshwater transports are estimated and compared with the output of the numerical models. The study is organized as follows: [Section 2](#) presents the hydrographic data acquired on the 1997, 2003 and 2012 cruises, the water masses distribution and the numerical models used. [Section 3](#) introduces the initial geostrophic velocity estimates, the unbalanced mass transports and the inverse modelling used to adjust them. Next, [Section 4](#) presents the result of the inverse box model and the adjusted geostrophic mass transports. [Section 5](#) relates the results obtained in terms of heat and freshwater fluxes and compares them with the outputs of the numerical models. Finally, [Section 6](#) discusses the results presented in sections 4 and 5.

## 2. Data

### 2.1. Hydrographic data

Hydrographic data from 1997, 2003 and 2012 were collected along the A20 section at nominally 52°W in the North Atlantic ([Fig. 1](#)). The sections were sampled in summer, fall and spring, respectively. The 1997 section was part of WOCE-WHP, while both the 2003 and 2012 sections were part of the successive international CLIVAR. The sampling direction changed between sections, starting in the north, and going south in 1997 and 2003, and *vice versa* in 2012. The northern tip of all transects is the Grand Banks of Newfoundland, while the southern edge

is Suriname's Exclusive Economic Zone (EEZ) for the 1997 and the 2003 occupations, and French Guiana's EEZ for the 2012 transect.

The data were collected using a rosette equipped with a Lowered Acoustic Doppler Current Profiler (LADCP), a Neil Brown Instrument Systems Mark III (NBIS MK3) Conductivity-Temperature-Depth sensor (CTD) for the 1997 occupation, and a SeaBird 911plus CTD for the other two occupations. In addition, Shipboard ADCP (SADCP) data were collected in each survey. A total of 95, 88 and 83 stations were sampled in 1997, 2003 and 2012, respectively. The 1997 survey lacks LADCP data on stations 1 to 4, 55, 57, 61 and 92 to 95. Likewise, the 2003 survey lacks LADCP data on stations 85 to 88.

Wind data from the National Center for Environmental Prediction Reanalysis II (NCEP-DOE) project from the National Oceanic and Atmospheric Administration (NOAA) are used to estimate Ekman transports for each survey ([Kanamitsu et al., 2002](#)).

A  $\theta$ - $S$  diagram for the southern part of the A20 section and the vertical distribution of potential temperature ( $\theta$ ) and salinity, together with neutral density ( $\gamma^{\rho}$ ; [Jackett and McDougall, 1997](#)) are shown in [Figs. 2, 3 and 4](#), respectively. These property distributions help to identify the reference level as in [Casanova-Masjoan et al. \(2018\)](#) and in [Joyce et al. \(2001\)](#). This reference level is then used to integrate the thermal wind equation and to calculate the transports between density layers. Moreover, the property characteristics are used also to assess the water mass distribution throughout the years. The water mass distribution in the A20 section ([Figs. 3 and 4, Table 1](#)) varies slightly from that given in [Casanova-Masjoan et al. \(2018\)](#) for the A22 section. The slight variations between the two sections are caused by their geographical location. The A22 section at 66°W is located west of A20 and it crosses the Antilles and samples part of the Caribbean Sea, A20 samples the western part of the

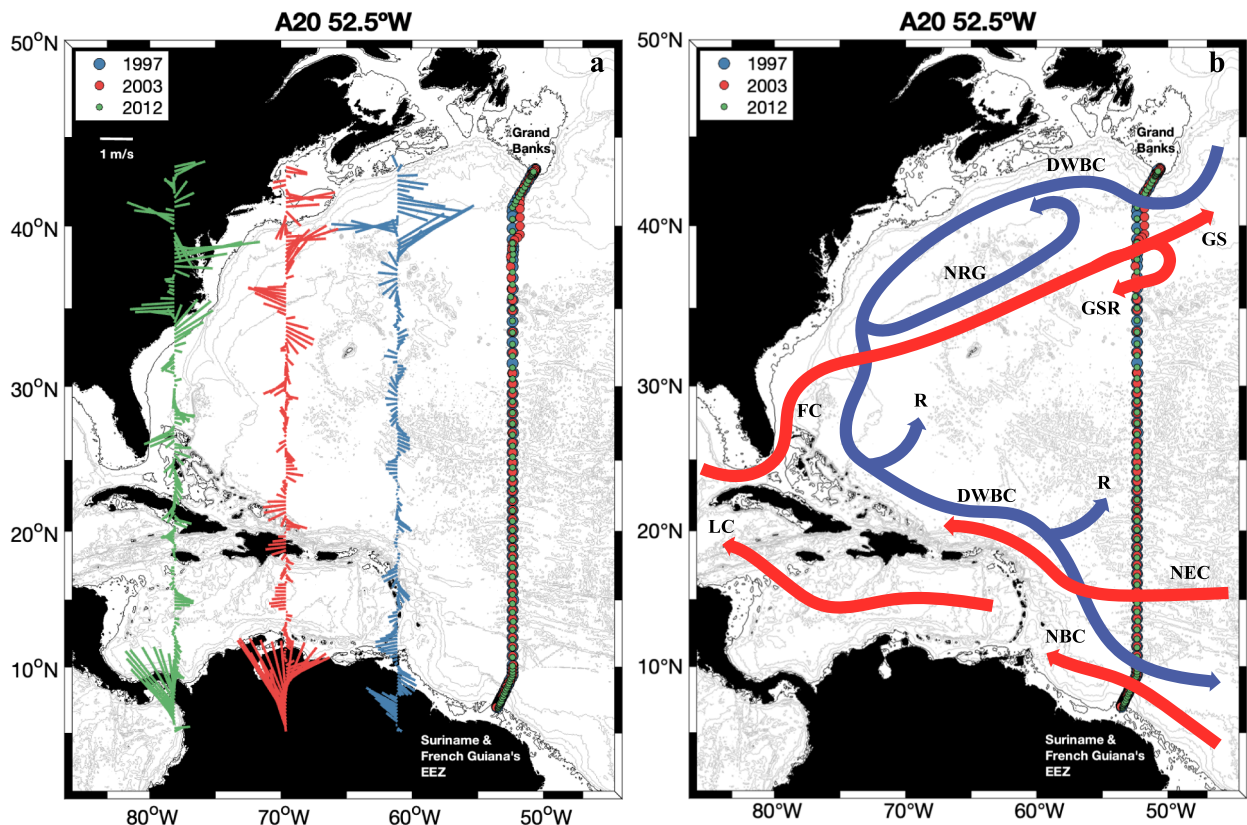


**Fig. 1.** a) Station positions carried out repeatedly at 52°W (A20) in 1997 (blue), 2003 (red) and 2012 (green). Sea surface velocities from the GLORYS model output at 52°W for 1997, 2003 and 2012 are presented shifted to the west to be better displayed. b) The main currents are represented in dark blue and red arrows for cold and warm currents, respectively. DWBC stands for Deep Western Boundary Current, NRG stands for Northern Recirculation Gyre, GS for Gulf Stream, GSR for Gulf Stream Recirculation, FC for Florida Current, R for Recirculation, LC for Loop Current, NEC for North Equatorial Current, and NBC for North Brazil Current (adapted from [Bower et al., 2019](#))

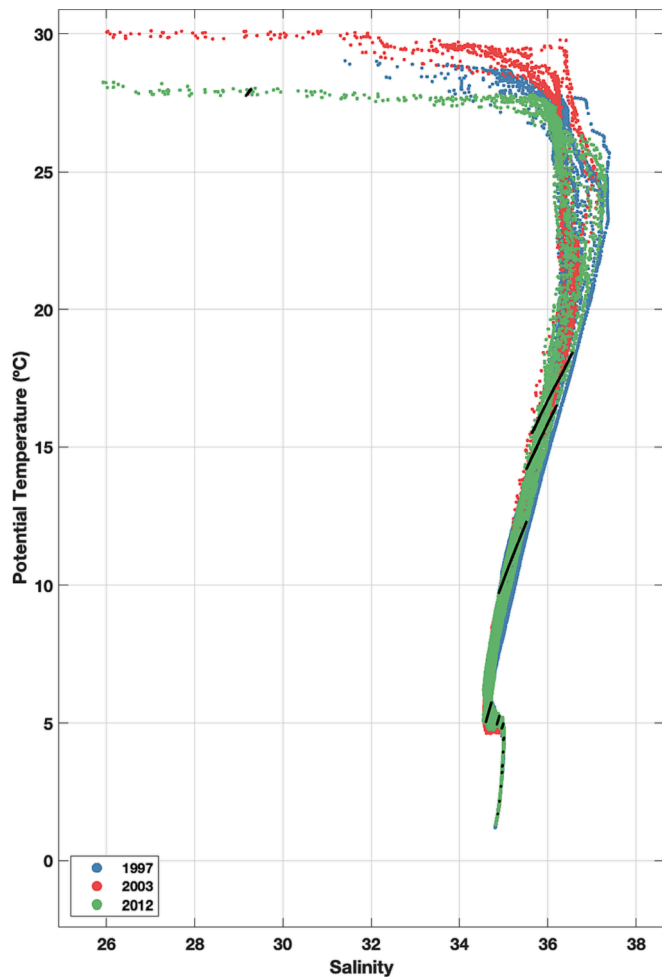


Fig. 2.  $\theta$ -S diagram of stations 60–90 (1997 and 2003) and 1–30 (2012) of the A20 hydrographic section at 52°W in the Atlantic Ocean. Blue, red and green dots are for 1997, 2003 and 2012, respectively. Black lines are the neutral density layers in which the ocean has been divided.

North Atlantic Subtropical Gyre. It also reaches further north than A22, extending all the way to the Grand Banks at 43°N. These geographical differences lead to the presence of more meridionally extended Antarctic

Intermediate Water (AAIW) and Antarctic Bottom Water (AABW) layers in A20 than in A22. AAIW appears as a distinguishable low salinity lobe of water in 250–1250 m depth range in the southern part of the A20 section (Fig. 4). AABW is a cool (<2°C) and low salinity (<34.88) water mass at the bottom of the ocean, below 4500 m depth (Figs. 3 and 4). Additionally, two freshwater masses appear in the first few meters of the water column both at the northernmost and southernmost tips of A20: Polar Surface Water (PSW) occupying from the surface to 250 m depth at the northern end of the section, and Amazonian runoff waters extending a few meters depth at the southern end only in 2003 and in 2012 (Figs. 2, 3 and 4). All three sections sampled the Subtropical Mode Water (STMW), which is formed by convection in late winter south of the GS (Joyce et al., 2013) with salinities in the range of 36–36.5 (Fig. 4). North Atlantic Subtropical UnderWater (STUW) appears as a maximum in salinity (>36.5) in the shallow layers on the southern side of the section, from 5°N to 15°N (Fig. 4). It is formed as the result of the positive result of evaporation-precipitation in the central tropical Atlantic (Worthington, 1976). Labrador Sea Water (LSW), the upper branch of the North Atlantic Deep Water (NADW), flows southward from the Labrador Sea into the study region. On A20, it is sampled at latitudes > 40°N and nominally at 750–1000 m depth (Figs. 3 and 4). Iceland-Scotland Overflow Water (ISOW) and Denmark Strait Overflow Water (DSOW), the lower branches of the NADW, can be found below LSW at 2500–4500 m depth. These three water masses form the NADW carried southward by the DWBC that flows to the South Atlantic Ocean after two crossings of the A20 section.

2.2. Numerical ocean model data

A free-running model and two data-assimilating models with monthly resolution are compared to the hydrographic observations to assess which provides the best match. After that, the best one is used to inform a study of the interannual variability existing between the cruises. The model products were obtained at 52°W, for latitudes between 5° and 50°N, and for the full water column.

The 6th version of the Modular Ocean Model (MOM) produced by the Geophysical Fluid Dynamics Laboratory (Adcroft et al., 2019) is a free running model. It has a nominal 1/4° horizontal resolution and 50 vertical levels. It is forced with the JRA55-do atmospheric reanalysis product (Stewart et al., 2020; Tsujino et al., 2020), yielding monthly averaged products for the years 1958–2018.

The “Estimating the Circulation and Climate of the Ocean Version 4 Release 4” (ECCOV4r4) model is a data-assimilating model produced by the Jet Propulsion Laboratory. Its vertical gridding varies from 10 m to

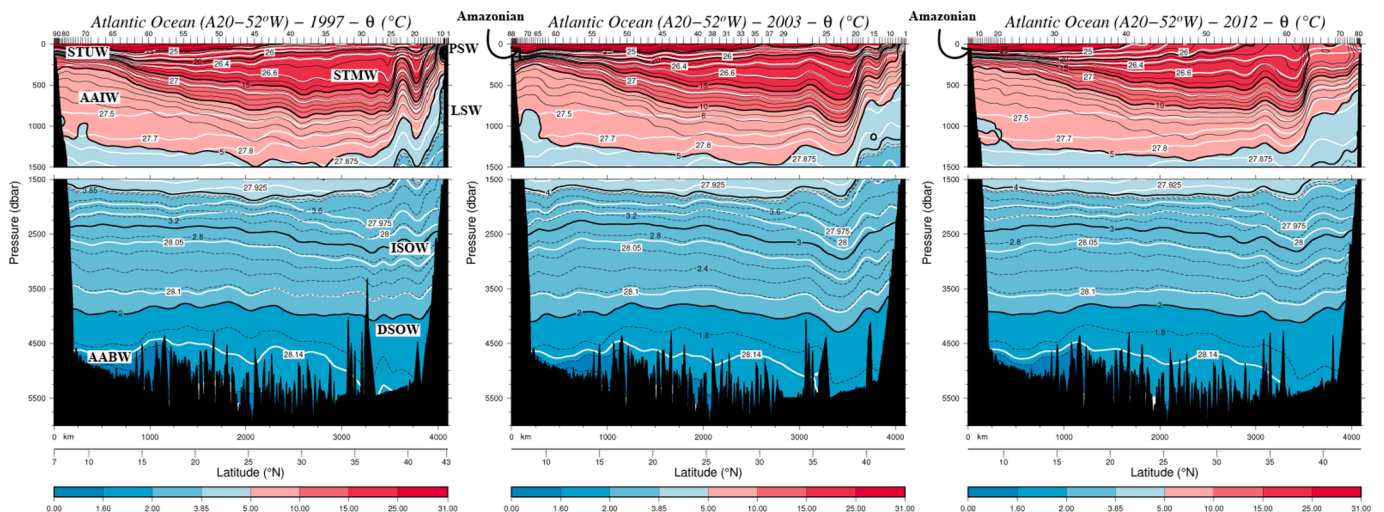


Fig. 3. Vertical sections of potential temperature ( $\theta$ , °C) at 52°W in the Atlantic Ocean for (a) 1997, (b) 2003 and (c) 2012. Neutral density ( $\gamma^n$ , kg m<sup>-3</sup>) is overlaid in white lines.

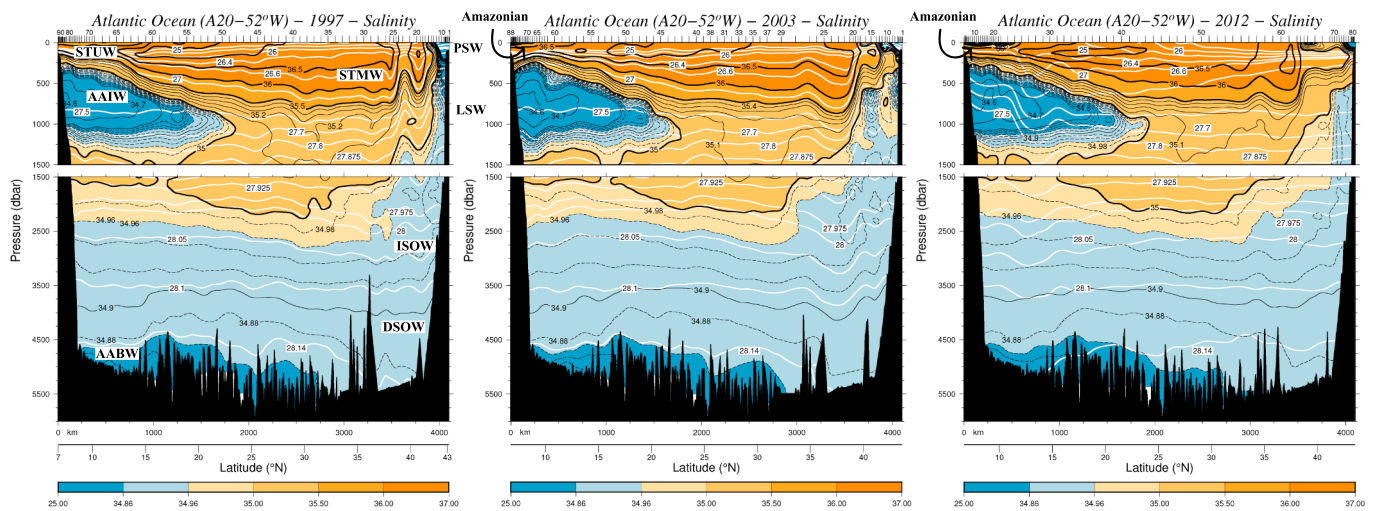


Fig. 4. Same as Fig. 2.2 but for salinity.

**Table 1**  
Neutral density layers and water masses. Level of no motion indicated in bold.

Layer	Neutral density ( $\gamma^n$ ) range	Water Mass
1	Surf.-26.4	STUW
2	26.4–26.6	STMW
3	26.6–27	AAIW
4	27–27.5	AAIW
5	27.5–27.7	AAIW
6	27.7–27.8	AAIW
7	27.8–27.875	LSW
8	27.875–27.925	LSW
9	27.925–27.975	LSW
10	27.975–28	ISOW
11	28–28.05	ISOW
12	28.05–28.1	DSOW
13	28.1– <b>28.14</b>	DSOW
14	<b>28.14</b> -bot.	AABW

457 m from the surface to the bottom. Its spatial horizontal resolution is  $1/2^\circ$  over the entire globe, whereas the temporal resolution used for this work is one month (Forget et al., 2015; Fukumori et al., 2021).

The “Global Ocean Physics Reanalysis” (GLORYS) model is a global ocean reanalysis and data-assimilating model produced by the Copernicus Marine Environment Monitoring Service. It describes ocean circulation at eddy-resolving resolution with a spatial resolution of  $1/12^\circ$  and a temporal resolution of one month, and the depth is gridded in 50 standard levels (Lellouche et al., 2018).

### 3. Geostrophic transport and inverse model

The initial geostrophic velocity is computed for each station pair using the thermal wind equation. Following Casanova-Masjoan et al. (2018) and Joyce et al. (2001), the neutral density level of  $\gamma^n = 28.14 \text{ kg m}^{-3}$  has been used as the reference layer to calculate the geostrophic velocity. This level lies between the eastward flowing NADW and the westward flowing AABW in section A20. When the seafloor is shallower than this layer, the closest common depth layer existing on the station pair is used as the reference level.

Additionally, the relative geostrophic velocity is adjusted to ADCP measurements following Comas-Rodríguez et al. (2010): the vertical profiles of the SADCP, LADCP and geostrophic velocities are visually compared at each station pair (Fig. 5). Then, an adjustment is made by selecting a depth interval where any of the ADCP velocities match the geostrophic velocity. When both SADCP and LADCP velocity profiles match with the geostrophic velocity, the SADCP profile is selected for

the adjustment. The SADCP vertical shear used for the comparison has been computed as suggested by E. Firing (personal communication): a range of 2 nautical miles from the CTD location is established for each CTD/LADCP station sampled. SADCP data sampled within this range is averaged and associated to that station. Velocities between two stations are averaged separately from the on-station velocity. Then, the SADCP velocity used for the comparison is computed as the average velocity between station  $n^{\text{th}}$ , station  $n^{\text{th}} + 1$  and the value between those two stations. This final value is taken as the best approximation of the SADCP vertical shear between station pairs. Fig. 5 shows several adjustments for 1997, 2003, and 2012 at the GS location. However, not every station pair has undergone the adjustment due to lack of a similarity pattern between the S/LADCP and the geostrophic velocity profiles. The ADCP uses the particles in the water column to measure the shear, hence when the water column is low backscattered (low particle concentration), the ADCP might not resolve the velocity shear appropriately.

The water column is divided into 14 neutral density layers (Table 1). Casanova-Masjoan et al. (2018), Hall (2004) and Joyce et al. (2001) used 17 layers, however the outcropping of several isopycnals in 2012 (Fig. 3c) forms a set of large artificial eddies when the inverse model is applied. Therefore, we combined several shallower layers including the outcropped layers to avoid this issue. The deeper layers are the same as those used in the above-mentioned studies (Table 1). The initial net mass imbalances are  $-7.4 \text{ Sv}$ ,  $57.0 \text{ Sv}$  and  $0.4 \text{ Sv}$  for 1997, 2003 and 2012, respectively. After the ADCP adjustments, the net mass imbalances increase to  $-8.2 \text{ Sv}$ ,  $62.8 \text{ Sv}$  and  $-10.4 \text{ Sv}$ , respectively (Fig. 6). The ADCP-adjusted overall distribution (red) presents some minor changes over the original distribution (blue). For 1997, the thermocline and intermediate transports ( $\gamma^n = 26.4 \text{ kg m}^{-3}$  to  $\gamma^n = 27.5 \text{ kg m}^{-3}$ ) decrease to almost zero, and the mass transport over the deep layers ( $\gamma^n = 28.1 \text{ kg m}^{-3}$  to  $\gamma^n = 28.14 \text{ kg m}^{-3}$ ) significantly increases. For 2003, the intermediate transport ( $\gamma^n = 27.0 \text{ kg m}^{-3}$  to  $\gamma^n = 27.5 \text{ kg m}^{-3}$ ) decreases while the deep transport ( $\gamma^n = 28.1 \text{ kg m}^{-3}$  to  $\gamma^n = 28.14 \text{ kg m}^{-3}$ ) increases. The vertical distribution does not change in 2012 except in the deep and bottom layers ( $\gamma^n = 28 \text{ kg m}^{-3}$  to the bottom), where the slightly eastward transport changes to westward transport.

After the use of ADCP data to estimate the new mass transport, an inverse model is applied to adjust the imbalance of the mass transport (Wunsch, 1996). The inverse model uses a set of constraints and uncertainties, with mass conservation being the most important constraint (Wunsch, 1996; Wunsch, 1978). The inverse model follows previous studies in the region (Casanova-Masjoan et al., 2018; Hall, 2004; Joyce et al., 2001) but with two major differences: the original 17 neutral density layers has been reduced to 14 layers, as explained before, and

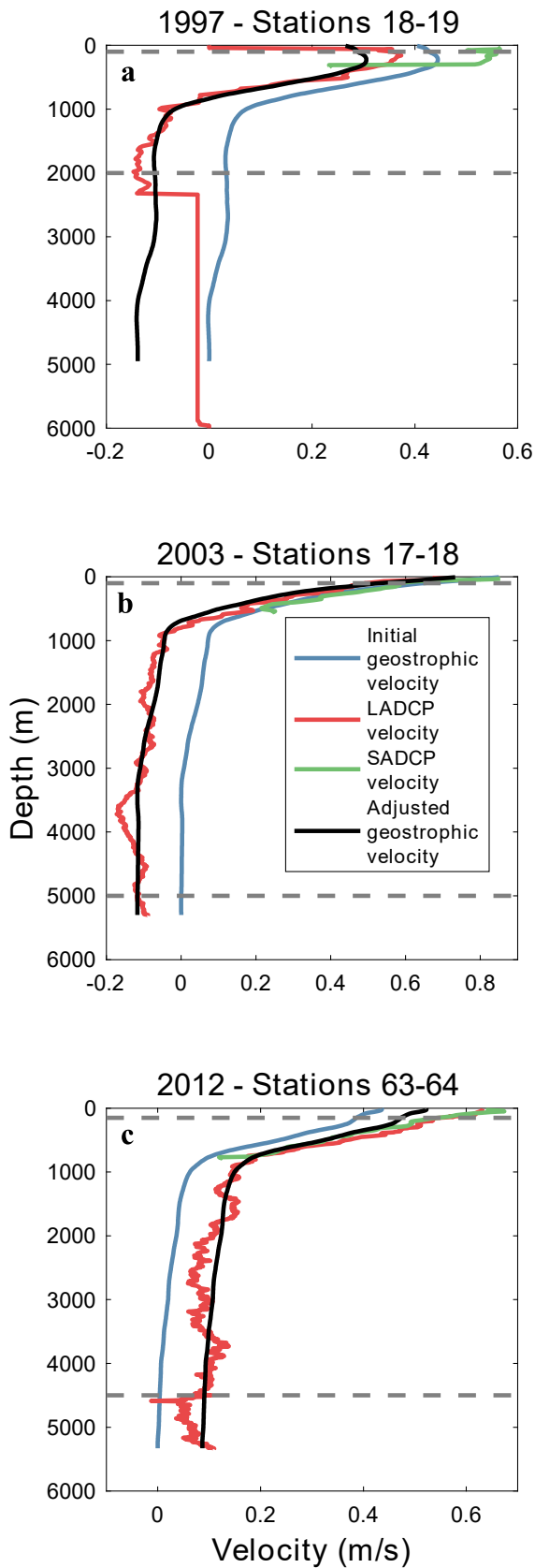


Fig. 5. Examples of comparison between the initial geostrophic velocity profile (blue line), the LADCP (red line) and SADCP (green line) velocities normal to station pairs and the geostrophic velocity profile adjusted to ADCP data (black line) for (a) 1997, (b) 2003 and (c) 2012. Gray dashed lines indicate the depth range where the adjustment is made. Axes range vary between figures.

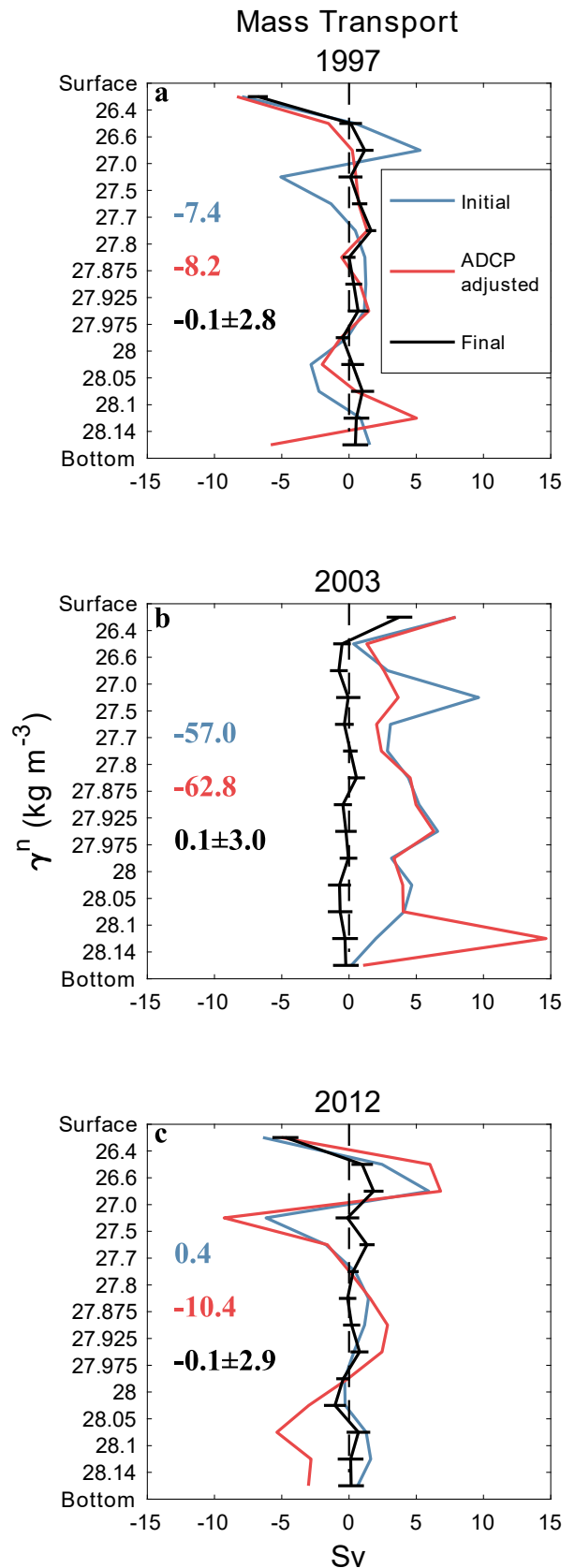


Fig. 6. Meridionally integrated mass transport (Sv) across the A20 section for (a) 1997, (b) 2003 and (c) 2012. Blue lines are the initial (unbalanced) mass transports, red lines are the ADCP (unbalanced) adjusted mass transports and black lines are the inverse model solution's derived mass transports. Total mass transports are shown in their respective colors.

the total silica conservation has not been included in the inverse model. Silica conservation has been achieved when imposing mass conservation ( $34.9 \pm 150.2$  Kmol/s,  $15.1 \pm 177.1$  Kmol/s and  $39.2 \pm 142.6$  Kmol/s for 1997, 2003 and 2012, respectively). Therefore, the silica conservation equations do not introduce independent equations.

The inverse problem is formulated as follows:

$$Ab + n = -Y.$$

where A is an  $M \times N_T$  matrix,  $N_T$  is the number of unknowns and M is the number of transport constraints. b is a column vector of length  $N_T$

( $N_T = N + 1$ ) containing the unknown geostrophic reference velocities for each of the  $N^{\text{th}}$  station pairs, plus the adjustment to the Ekman transport. n is a column vector of length M of the noise of each constraint. Y is a column vector of length M representing the mass transport initially unbalanced in each layer.

The inverse problem is solved through the Gauss–Markov method (Wunsch, 1996), which provides a solution for the initial estimates with minimum error variances. This method requires a priori variances for the velocities and the constraints. Following Joyce et al. (2001), the

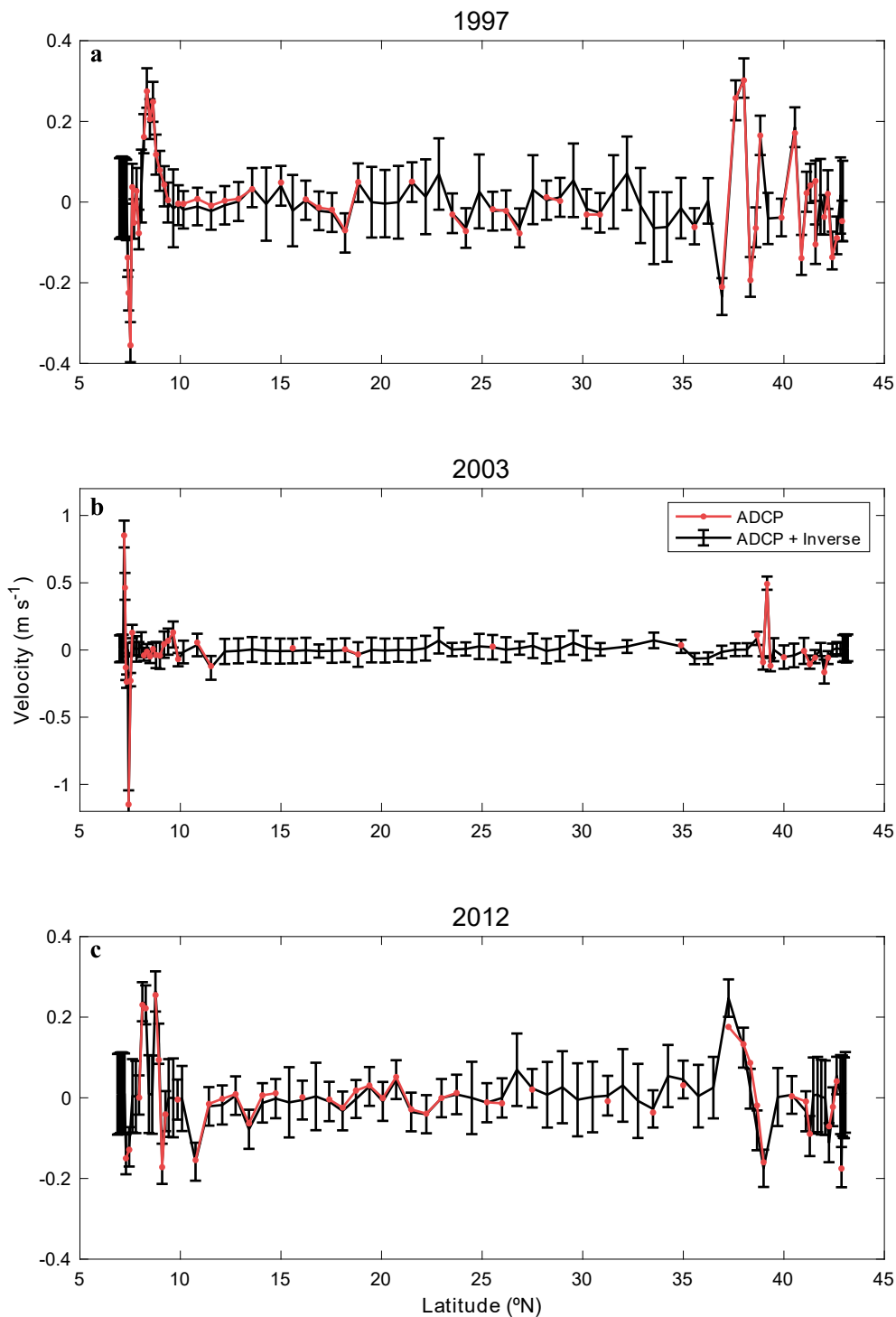


**Fig. 7.** ADCP-adjusted geostrophic velocity (red line) and ADCP-adjusted velocity plus the reference level velocity estimated from the inverse model (black line) versus latitude for (a) 1997, (b) 2003 and (c) 2012. Black error bars correspond to inverse modeling calculations. Gaps in the ADCP-adjusted velocity correspond to station pairs where the initial geostrophic velocity could not be adjusted to ADCP velocity. The 2003 y-axis has a different range than for 1997 and 2012.

chosen velocity variances are  $(0.05 \text{ m s}^{-1})^2$  for the ADCP-adjusted velocities and  $(0.1 \text{ m s}^{-1})^2$  for the non-ADCP-adjusted velocities. The mass variances are  $(0.5 \text{ Sv})^2$  for the total mass conservation,  $(2 \text{ Sv})^2$  for the shallowest layer and  $(1 \text{ Sv})^2$  for the remaining layers.

The inverse model is applied to the water volume enclosed by the American continent coastline and the A20 section to the east. There is not a significant flow through the Panama Canal (Joyce et al., 2001), and, therefore, the water volume is fully enclosed. The sum of the

velocities at the reference level (with their error estimates) from the inverse model plus the ADCP velocities are presented in Fig. 7 (black). The added ADCP velocities are represented in red. Both velocities show a similar distribution: features like the DWBC and the GS velocities are remarkably different from zero while the ocean interior shows velocities not significantly different from zero. This set of velocities adjusted from the ADCP and from the inverse model are used to calculate the adjusted mass, heat and freshwater transports.

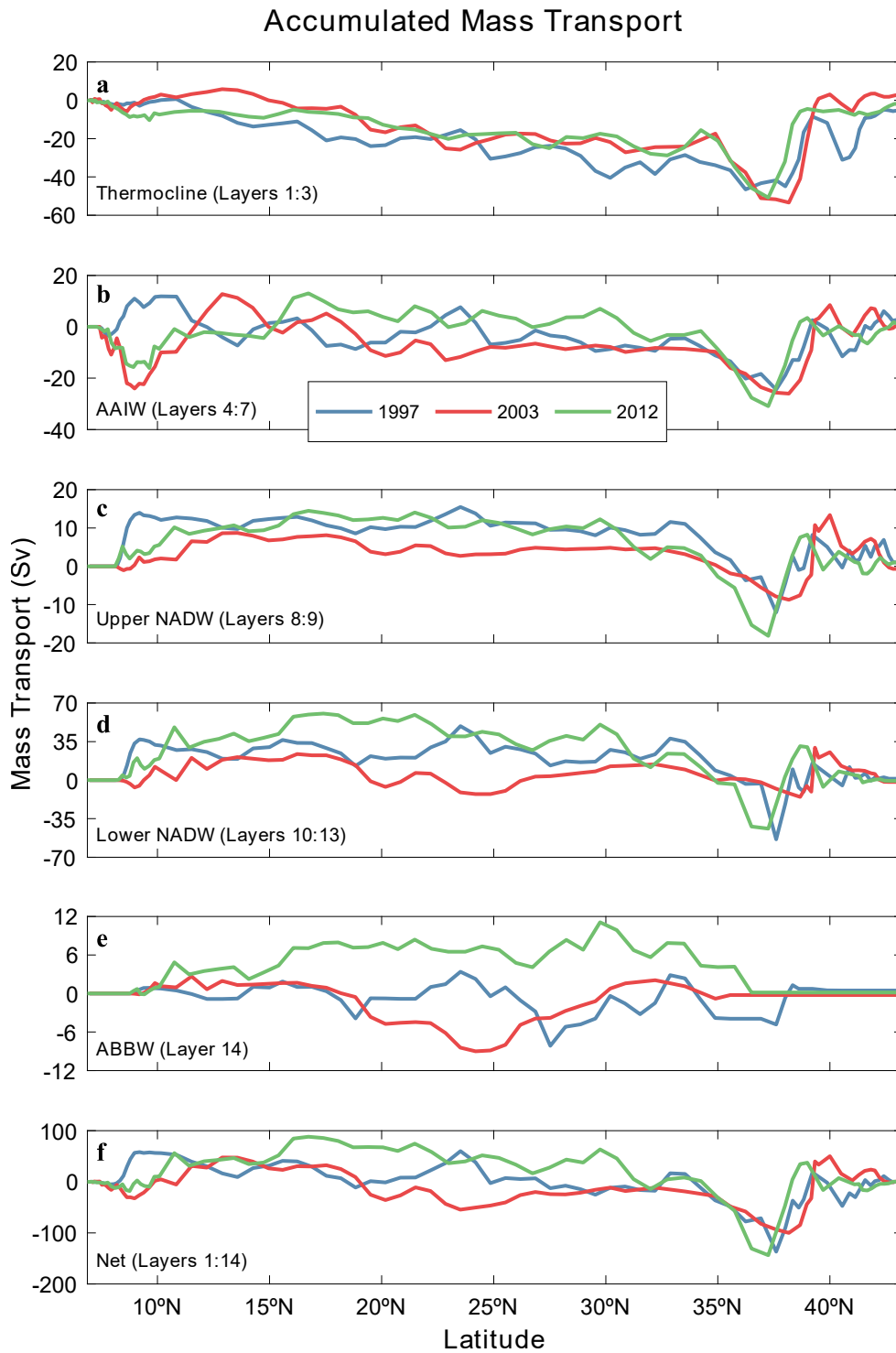


**Fig. 8.** Northward accumulated mass transport (Sv) after the inverse model for 1997 (blue), 2003 (red) and 2012 (green) occupations. (a) Thermocline transport estimated for layers 1 to 3. (b) AAIW transport estimated for layers 4 to 7. (c) Upper NADW transport estimated for layers 8 to 9. (d) Lower NADW transport estimated for layers 10 to 13. (e) AABW transport estimated for layer 14. (f) Net transport estimated for layers 1 to 14. Y-axis range varies between subplots.

#### 4. Adjusted geostrophic transport

The zonal mass transport per neutral density layer with its net imbalance is shown in Fig. 6. The inverse model has reduced the ADCP-adjusted imbalances to values not significantly different from zero ( $-0.1 \pm 2.8$  Sv,  $0.1 \pm 3.0$  Sv and  $-0.1 \pm 2.9$  Sv for 1997, 2003 and 2012, respectively). The shallowest layer of the zonal transport presents a westwards imbalance in both 1997 ( $-6.8 \pm 0.7$  Sv) and 2012 ( $-4.7 \pm 1.0$  Sv), and eastwards in 2003 ( $3.7 \pm 1.0$  Sv). The zonal transport distribution through latitudes and density layers provides the variability of mass transport of the main currents of the AMOC (Fig. 8). Ocean General Circulation Models (OGCMs) are used to determine the most reliable mass transports compared to hydrographic data (Figs. 9, 10 and 11) and to estimate the time variation of heat and freshwater transports.

The North Brazil Current (NBC) flows between the southernmost station pair and  $7.7/7.8^\circ\text{N}$  in 1997/2003. The northern limit of the current extends to  $8.3^\circ\text{N}$  in 2012 (Figs. 1 and 8a, b). We have considered the northern limit of the NBC as the starting location of the eastward flow as seen in Fig. 1. The NBC extends from the surface to  $\gamma^n = 27.7$  kg  $\text{m}^{-3}$  ( $\sim 1100$  m depth) in all surveys. The NBC mass transport (Table 2) presents a minimum in 1997 ( $-5.6 \pm 0.7$  Sv) followed by an intensification in 2003 ( $-15.8 \pm 1.2$  Sv) and a non-significant change in 2012 ( $-15.6 \pm 1.6$  Sv). The OGCMs outputs resemble the hydrographic NBC differently in each survey. The MOM and ECCO outputs only resemble the hydrographic NBC in 1997, where the GLORYS output presents a stronger NBC (Fig. 9a). However, the 2003 (Fig. 10a) and 2012 (Fig. 11a) MOM and ECCO outputs do not match the NBC, but the GLORYS output does.

North of the NBC, the NEC flows westward between the surface and  $\gamma^n = 27$  kg  $\text{m}^{-3}$  ( $\sim 500$  m depth). The NECs northern limit is considered at approximately  $24.2^\circ\text{N}$ ,  $25.5^\circ\text{N}$  and  $25.2^\circ\text{N}$  for 1997, 2003 and 2012, respectively (Fig. 8a). This flow is fed by the southern branches of the Azores Current and the Canary Current (Hernández-Guerra et al., 2002; Stramma, 1984). The northernmost part of this westward flow is called

Antilles Current when flowing north of the Puerto Rico Island (Bryden et al., 2005; Hernández-Guerra et al., 2010; Johns et al., 2008). The northern limit of the NEC has been chosen as the latitude where the mass transport of the GSR is not significantly different than zero ( $-2.0 \pm 3.8$ ,  $0.1 \pm 4.0$  and  $1.4 \pm 4.0$  Sv in 1997, 2003 and 2012, respectively). The NEC mass transport weakens between 1997 and 2003 ( $-28.6 \pm 2.5$  Sv and  $-12.3 \pm 3.6$  Sv, respectively) and stays with a similar mass transport to that of 2003 in 2012 ( $-10.6 \pm 2.8$  Sv) (Table 2). The NEC estimated from the OGCMs resembles the pattern of the NEC circulation from hydrography, showing stronger mesoscale patterns in the in-situ data (Figs. 9a, 10a and 11a).

The GSR and GS mass transports are computed between the surface and the ocean bottom. The latitudinal ranges of the GSR are  $32.9\text{--}36.9^\circ\text{N}$ ,  $34.9\text{--}38.2^\circ\text{N}$  and  $34.2\text{--}37.3^\circ\text{N}$  for 1997, 2003 and 2012, respectively (Fig. 8f). Thus, the GSR width (445, 367 and 345 km in 1997, 2003 and 2012, respectively) presents a narrowing between each survey, and its location shifts to the north in 2003 compared to 1997 and 2012. The mass transport of the GSR is  $-152.1 \pm 17.0$  Sv,  $-72.3 \pm 17.4$  Sv and  $-145.3 \pm 19.8$  Sv in 1997, 2003 and 2012, respectively (Table 2). The significant weakening in 2003 compared to 1997 and 2012 is also observed in the GS mass transports ( $155.3 \pm 11.1$  Sv,  $102.7 \pm 13.5$  Sv and  $181.1 \pm 14.9$  Sv for 1997, 2003 and 2012, respectively). Moreover, the GS also presents a northern shifting in 2003 ( $38.2\text{--}41.0^\circ\text{N}$ ) compared to 1997 ( $36.9\text{--}38.8^\circ\text{N}$ ) and 2012 ( $37.3\text{--}38.9^\circ\text{N}$ ; Fig. 8f). However, the GS does not follow the same narrowing present in the GSR because it is wider in 2003 (311 km) than in 1997 (212 km) and 2012 (178 km). The GSR and GS from the OGCMs outputs show lower mass transports than the hydrographic results (Figs. 9d, 10d and 11d). The GSR mass transport from the OGCMs output and from 1997, 2003 and 2012 are 3.6, 13.0, 6.0 Sv (MOM), 20.6, 12.3, 3.0 Sv (ECCO) and  $-73.8$ ,  $-17.6$ ,  $-32.2$  Sv (GLORYS), respectively. The results for the GS are 0.4, 6.9,  $-11.4$  Sv (MOM), 28.2, 0.6, 1.4 Sv (ECCO) and 182.3, 24.2, 84.7 Sv (GLORYS), respectively. Only the GLORYS output resembles the pattern of circulation of the GS system (Fig. 9d).

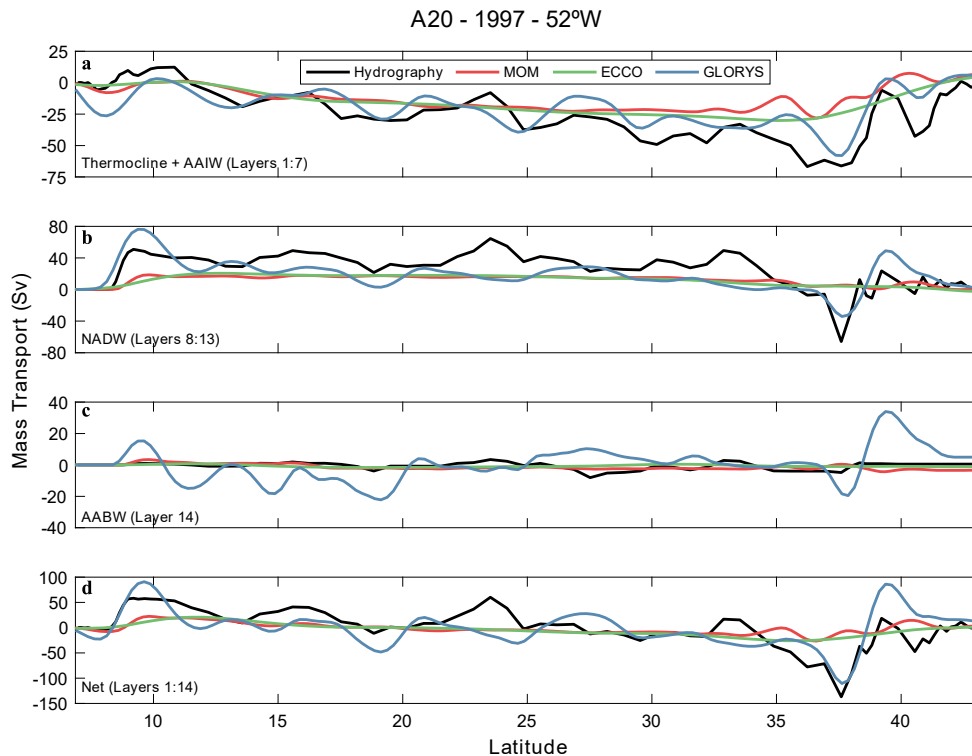


Fig. 9. Northward accumulated mass transport (Sv) after the inverse model (black), from the MOM model (red), from the ECCO model (green) and from the GLORYS model (blue) for 1997. (a) Thermocline and AAIW transport estimated for layers 1 to 7. (b) NADW transport estimated for layers 8 to 13. (c) AABW transport estimated for layer 14. (d) Net transport estimated for layers 1 to 14. Y-axis range varies between subplots.

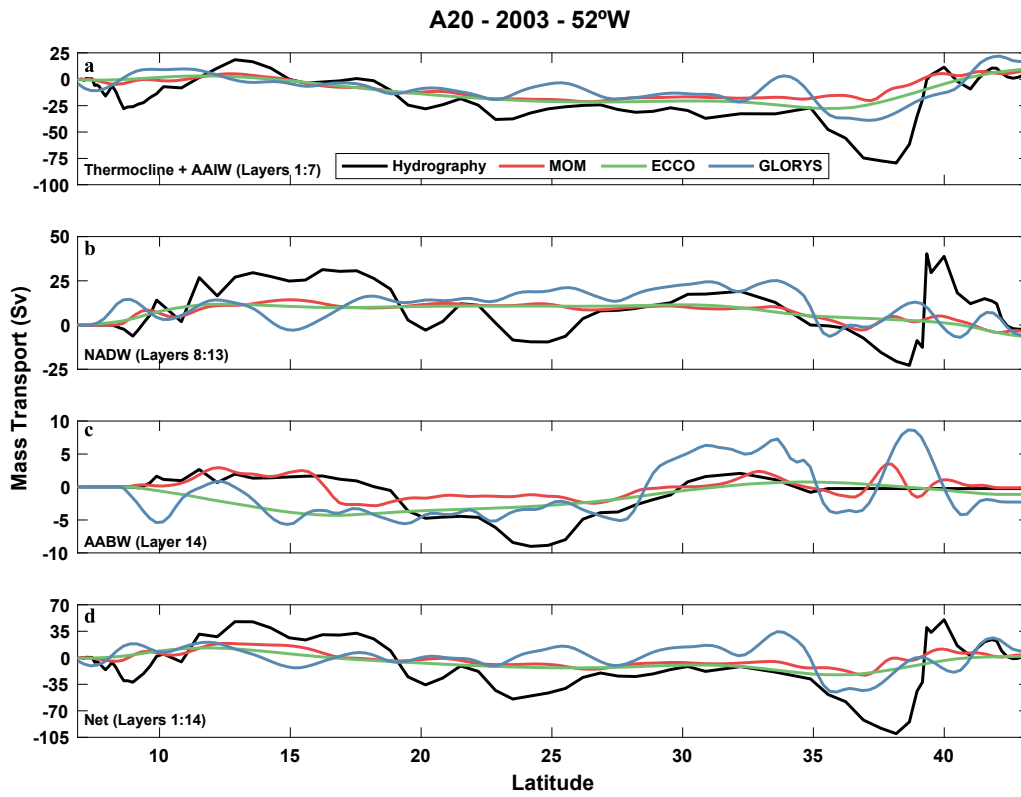


Fig. 10. Same as Fig. 9 but for 2003.

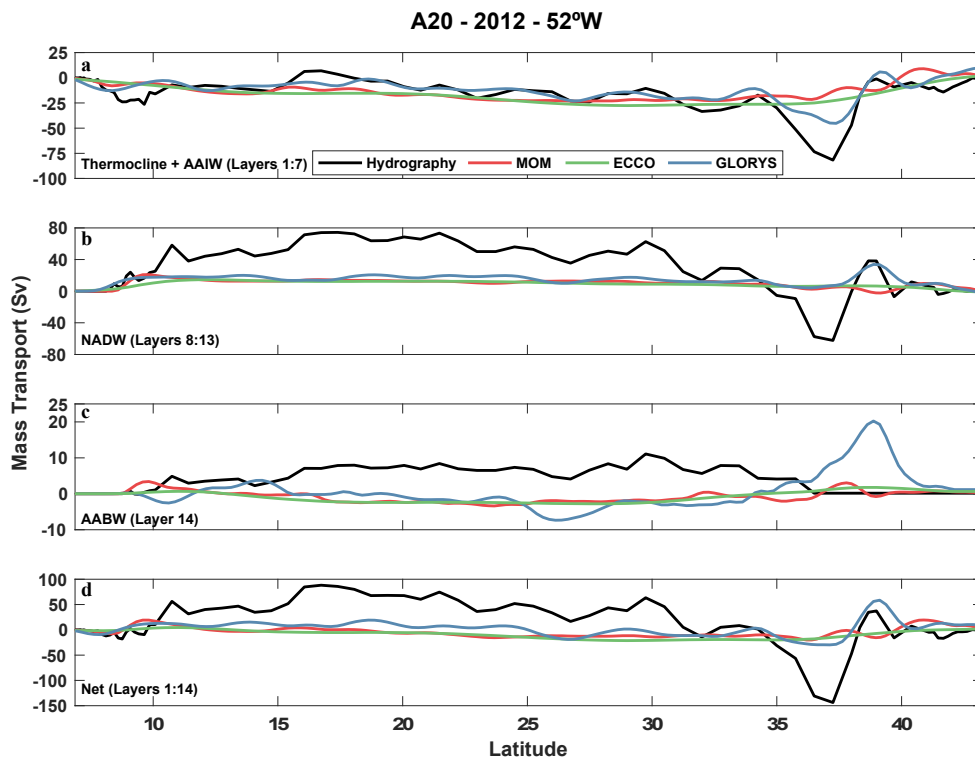


Fig. 11. Same as Fig. 9 but for 2012.

The DWBC flows at deep layers ( $\gamma^n = 27.875 \text{ kg m}^{-3}$  to  $\gamma^n = 28.14 \text{ kg m}^{-3}$ ) and crosses the northern/southern boundaries at the latitudinal ranges of 39.2–42.8/8.1–13.6°N, 41.0–42.8/8.2–14.1°N and 38.9–42.8/

8.1–14.1°N for 1997, 2003 and 2012, respectively (Fig. 8c, d). In the northern crossing, the DWBC presents a narrowing in 2003 (200 km) compared to 1997 (401 km) and 2012 (434 km). In the southern

**Table 2**

Mass transports, latitude range and layers of the main currents of the A20 section in 1997, 2003 and 2012.

	Layers	Latitude Range (°N)			Transports (Sv)		
		1997	2003	2012	1997	2003	2012
GS	1:14	36.9–38.8	38.2–41.0	37.3–38.9	155.3 ± 11.1	102.7 ± 13.5	181.1 ± 14.9
GSR	1:14	32.9–36.9	34.9–38.2	34.2–37.3	−152.1 ± 17.0	−72.3 ± 17.4	−145.3 ± 19.8
NBC	1:5	7.0–7.7	7.0–7.8	6.9–8.3	−5.6 ± 0.7	−15.8 ± 1.2	−15.6 ± 1.6
NEC	1:3	7.7–24.2	7.8–25.5	8.3–25.2	−28.6 ± 2.5	−12.3 ± 3.6	−10.6 ± 2.8
Upper North DWBC	8:9	39.2–42.8	41.0–42.8	38.9–42.8	−7.2 ± 3.1	−3.9 ± 4.3	−7.3 ± 3.5
Lower North DWBC	10:13	39.2–42.8	41.0–42.8	38.9–42.8	−14.0 ± 8.4	−10.5 ± 9.9	−30.6 ± 9.6
Net North DWBC	8:13	39.2–42.8	41.0–42.8	38.9–42.8	−21.2 ± 8.9	−14.4 ± 10.8	−37.9 ± 10.2
Upper South DWBC	8:9	8.1–13.6	8.2–14.1	8.1–14.1	9.8 ± 2.0	1.9 ± 2.1	9.2 ± 2.2
Lower South DWBC	10:13	8.1–13.6	8.2–14.1	8.1–14.1	19.3 ± 8.9	12.2 ± 7.8	35.3 ± 9.6
Net South DWBC	8:13	8.1–13.6	8.2–14.1	8.1–14.1	29.0 ± 9.1	14.2 ± 8.1	44.5 ± 9.8
Net	1:14	6.9–43.3	6.9–43.3	6.9–43.1	−0.1 ± 2.8	0.1 ± 3.0	−0.1 ± 2.9

crossing, the DWBC exhibits a widening from 1997 (612 km) to 2003 (657 km) which maintains to 2012 (668 km). The estimations of the DWBC mass transports at the northern/southern crossing are  $-21.2 \pm 8.9/29.0 \pm 9.1$  Sv,  $-14.4 \pm 10.8/14.2 \pm 8.1$  Sv and  $-37.9 \pm 10.2/44.5 \pm 9.8$  Sv for 1997, 2003 and 2012, respectively (Table 2). The northern-crossing DWBC from hydrography is only well represented by the GLORYS output with mass transports of  $-39.5$  (1997),  $-5.8$  (2003) and  $-33.8$  (2012) Sv (Figs. 9b, 10b and 11b). All three OGCM outputs present a weaker southern-crossing DWBC (Figs. 9b, 10b and 11b) than the obtained from hydrography, except the GLORYS output in 1997 (Fig. 9b).

The bottom transport of the AABW is computed between the neutral density layer  $\gamma^n = 28.14 \text{ kg m}^{-3}$  ( $\sim 4750$  m depth) and the bottom of the

ocean ( $\sim 5500$  m depth). Its southern edge is in all cases  $7.0^\circ\text{N}$ , but its northern edge shifts to the south between 1997 ( $27.5^\circ\text{N}$ ) and 2003 ( $24.2^\circ\text{N}$ ) (Fig. 8e). It flows westwards with a mass transport of  $-8.1 \pm 7.0$  Sv and  $-9.0 \pm 7.9$  Sv in 1997 and 2003, respectively. Layers 13 ( $\gamma^n = 28.1 \text{ kg m}^{-3}$ ) and 14 ( $\gamma^n = 28.14 \text{ kg m}^{-3}$ ) appear to be coupled in 2012 as they present a similar pattern. Therefore, there is not a mean westward flow in layer 14 (Fig. 8e) to define and estimate the mass transport of AABW crossing the 2012 hydrographic section. The OGCM outputs present a very weak transport, almost nonexistent, of the AABW (Figs. 9c, 10c and 11c).

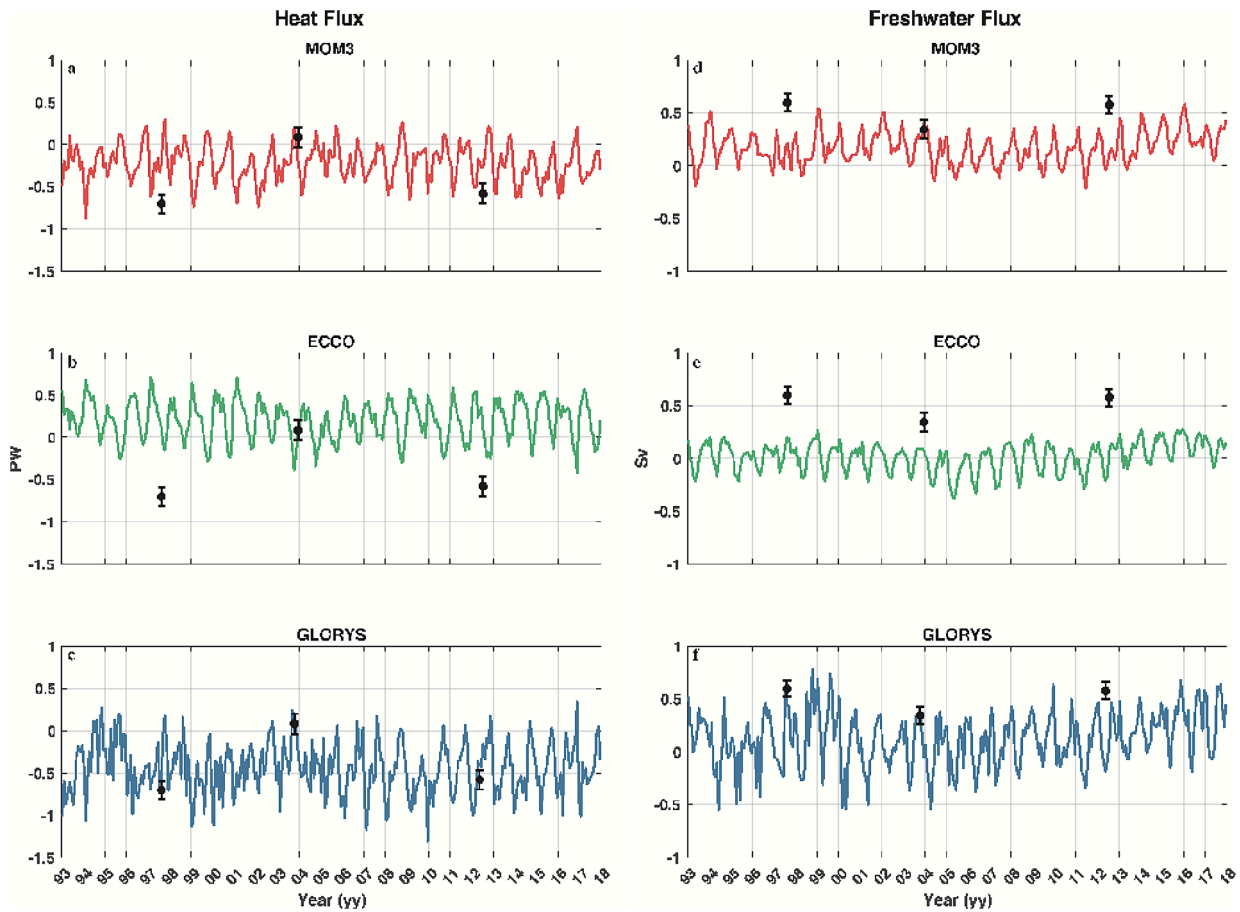


**Fig. 12.** Time series of heat (PW) and freshwater (Sv) fluxes between 1993 and 2018 estimated from the MOM (a, d, red line), ECCO (b, e, green line) and GLORYS (c, f, blue line) models. Black dots with error bars represent the values estimated from the inverse model in the month-year when the hydrographic section was carried out.

### 5. Heat and freshwater transports

The heat transport across our section is estimated from the inverse box model results:

$$\bar{H} = \sum_i \sum_j c_{p_{ij}} \rho_{ij} \Delta T_{ij} y_{ij} z_{ij} u_{ij}$$

where H is the net heat transport across the A20 section,  $c_{p_{ij}}$  is the specific heat capacity in layer i at station pair j,  $\rho_{ij}$  is the potential temperature,  $\rho_{ij}$  is the density,  $y_{ij}$  is the distance between adjacent stations,  $z_{ij}$  is the vertical distance between adjacent layers and  $u_{ij}$  is the perpendicular velocity to the A20 section from the inverse model.

In 1997 and 2012, the heat flux is to the west and with similar transports ( $-0.7 \pm 0.1$  PW and  $-0.6 \pm 0.1$  PW, respectively; 1 PW =  $10^{15}$  W). This results in a heat transport from the ocean to the atmosphere. In contrast, 2003 presents a non-significant heat transport ( $0.1 \pm 0.1$  PW). Fig. 12a, b and c presents the heat transport from OGCM outputs together with the heat transport estimated in each survey. Heat transports estimated by MOM3 and ECCO are higher than those estimated from the hydrographic cruises in 1997 and 2012 (Fig. 12a and b). The 2003 heat flux of the survey is the only result that lies within the MOM3 and ECCO ranges. On the other hand, heat transports estimated from GLORYS roughly match the heat transport estimated from hydrography, being  $-0.6$  PW,  $0.2$  PW and  $-0.4$  PW in 1997, 2003 and 2012, respectively (Fig. 12c and Table 3).

The monthly mean heat flux and standard deviation is computed from the GLORYS time series (Fig. 13a). The monthly mean heat flux is always negative providing heat from the ocean to the atmosphere. Additionally, a Mann-Kendall Tau test is applied to the GLORYS output to assess the trend over the 1993–2020 period (Fig. 13b). The result of this test shows that the heat flux presents a trend of  $-2.6 \times 10^{-2}$  PW per decade over the period with a confidence level of 72.1%. However, the heat flux does not show a significant trend when the confidence level is 95%.

The understanding of the global water cycle and the climate variability can be improved by the knowledge obtained in enclosed oceanographic sections. Specifically, the freshwater flux shows the air-sea interactions of the waters enclosed by an oceanographic section. In this work, the freshwater fluxes of the three surveys are estimated as in Joyce et al. (2001):

$$\bar{F} = - \sum_i \sum_j T_{ij} S'_{ij} / S_0$$

where F is the excess of precipitation plus runoff over evaporation in the closed volume,  $T_{ij}$  is the mass transport in layer i at station pair j, from the inverse model,  $S_0$  is the mean salinity and  $S'_{ij} = S_{ij} - S_0$ .

The resulting freshwater fluxes ( $0.6 \pm 0.1$ ,  $0.3 \pm 0.1$  and  $0.6 \pm 0.1$  Sv in 1997, 2003 and 2012, respectively) may be coupled with the heat fluxes, as they weaken and strengthen in the same surveys. The results provide that the precipitation and river runoff are higher than the evaporation for these surveys. As in heat flux, the freshwater flux from MOM3 and ECCO at the time of the cruises are different than those from the cruises (Fig. 12d and e). As in heat flux, the GLORYS output coincides with the freshwater flux from hydrography in 1997 (0.5 Sv) and

**Table 3**

Heat and freshwater fluxes from inverse calculations and from MOM, ECCO and GLORYS models for A20 in 1997, 2003 and 2012.

	Heat (PW)			Freshwater (Sv)		
	1997	2003	2012	1997	2003	2012
Hydrography	-0.7 ± 0.1	0.1 ± 0.1	-0.6 ± 0.1	0.6 ± 0.1	0.3 ± 0.1	0.6 ± 0.1
MOM	-0.2	0.0	-0.2	0.2	0.3	0.0
ECCO	-0.1	0.1	-0.2	0.2	0.1	-0.2
GLORYS	-0.6	0.2	-0.4	0.5	0.3	-0.1

2003 (0.3 Sv) although it is significantly different in 2012 (-0.1 Sv) (Table 3; Fig. 12f).

The monthly mean freshwater transport and its trend in the time series has been estimated from GLORYS following the same procedure used for the heat flux (Fig. 13c and d). The freshwater flux from the GLORYS output presents positive values except in spring, which means that overall, there is more precipitation and runoff than there is evaporation in the closed volume except in spring, when it reverses. A Mann-Kendall test applied to the freshwater flux estimated by the GLORYS output (Fig. 13d) provides a trend of  $8.1 \times 10^{-2}$  Sv per decade over that period with a confidence level of 99.9%, which is a more reliable result than the heat flux result. These results document an increase of precipitation in the area bounded by the section A20 at 52°W and the North, Central and South American continents from 1993 to 2020.

### 6. Discussion

The main currents and the heat and freshwater fluxes across the A20 section (52°W) in 1997, 2003 and 2012 have been investigated. In addition, the OGCMs outputs have been compared to the hydrographic results to find which one presents a better match and to estimate the seasonal and interannual variability of the heat and freshwater fluxes.

At the southernmost part of the A20 section, the NBC presents a high variability between summer (1997,  $-5.6 \pm 0.7$  Sv) and fall/spring (2003/2012,  $-15.8 \pm 1.2$  Sv/ $-15.6 \pm 1.6$  Sv). All three results are within the mass transport range  $-10$  to  $-30$  Sv estimated by Garzoli (2004) from continuous measurements between 2 and 3°N and 47.4–47.1°N. The NEC mass transport presents an opposite behavior compared to the NBC mass transport. The NEC is stronger in summer (1997,  $-28.6 \pm 2.5$  Sv) than in fall (2003,  $-12.3 \pm 3.6$  Sv) and in spring (2012,  $-10.6 \pm 2.8$  Sv). Using the Sverdrup relation, Hellerman (1980) estimated a NEC mass transport of  $-9$  Sv in fall and  $-23$  Sv in spring. The lack of an error estimate and the fact that these results were obtained at 38°W may explain the difference in the results.

The GS system (GSR/GS) presents an oscillatory behavior of weakening and strengthening of its mass transports between the pair of surveys 1997–2003 (summer:  $-152.1 \pm 17.0/155.3 \pm 11.1$  Sv; fall:  $-72.3 \pm 17.4/102.7 \pm 13.5$  Sv) and 2003–2012 (spring,  $-145.3 \pm 19.8/181.1 \pm 14.9$  Sv). In addition, the GS system is in its northernmost position in fall (2003, 38.2–41.0°N) compared to summer (1997, 36.9–38.8°N) and spring (2012, 37.3–38.9°N), which coincides with the results of Lee and Cornillon, (1995); Pérez-Hernández and Joyce, (2014); Rayner et al., (2011); Tracey and Watts, (1986); Sato and Rossby, (1995).

The mass transport of the northern/southern-crossing DWBC does not significantly change between summer (1997,  $-21.2 \pm 8.9/29.0 \pm 9.1$  Sv) and fall (2003,  $-14.4 \pm 10.8/14.2 \pm 8.1$  Sv). However, the mass transport of the DWBC is stronger in spring (2012,  $-37.9 \pm 10.2/44.5 \pm 9.8$  Sv). Comparing these results with those from Toole et al. (2011) and Toole et al. (2017) at Line W, all of them are within their mass transport range of  $-79.9$  Sv to  $-3.5$  Sv obtained with data ranging 2004–2014. As Le Bras et al. (2019) suggests, the NASG may respond to forcing through fast barotropic adjustments. Furthermore, Meinen & Garzoli (2014) found that the temporal variability of the DWBC at 26.5°N and 75°W is caused by Baroclinic Rossby Waves. The dominant period of these events is 70–90 days. Nevertheless, mass transport variations are observed in both larger and shorter time periods (Meinen and Garzoli, 2014).

The comparison of the mass transport from OGCM outputs with the mass transport from hydrographic data reveals that only the GLORYS model resembles the main currents studied in this work. In addition, the mass transport from MOM and ECCO numerical models present different estimations than the results obtained from the hydrography. This result may be caused by how each OGCM has been developed. The MOM model is a free-running model with no assimilation of data. GLORYS is a reanalysis model with assimilation of data and, in contrast, ECCO only assimilates data. Moreover, different parametrizations of physical processes, rates of mixing and the finer spatial resolution of the GLORYS (1/

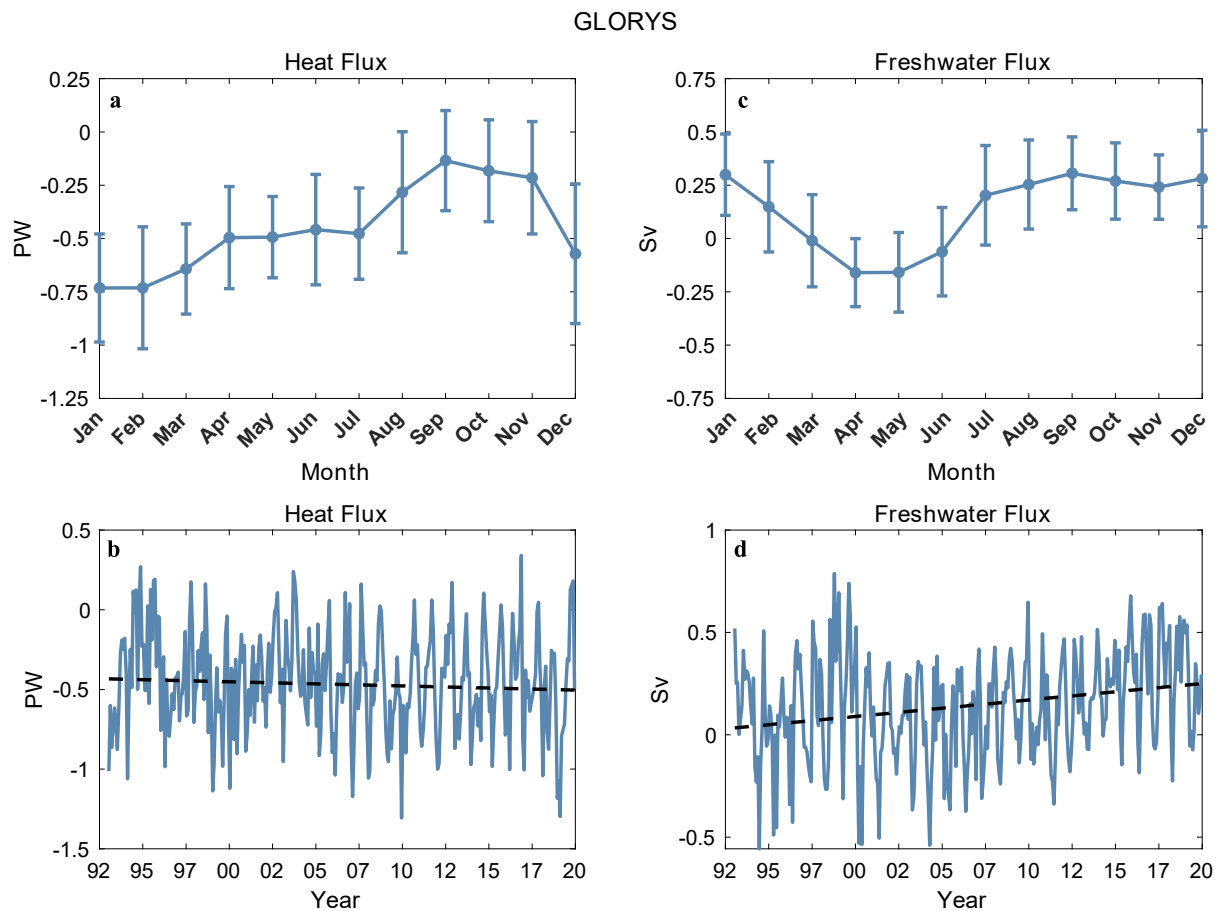


Fig. 13. Monthly mean and time series of heat (a, b; PW) and freshwater (c, d; Sv) fluxes estimated from the GLORYS model. Black thick dashed lines in (b) and (d) indicate the trend of the time series.

12° compared to 1/2° for ECCO and 1/4° for MOM) are responsible of the best fit to the observations.

The 1997 and 2012 heat fluxes are a net exchange from the ocean to the atmosphere ( $-0.7 \pm 0.1$  PW and  $-0.6 \pm 0.1$  PW, respectively). In contrast, the 2003 heat flux presents a non-significant transport ( $0.1 \pm 0.1$  PW). These results agree with the variability shown in the GLORYS heat flux. The monthly mean heat flux is always negative. This implies that the basin enclosed by the A20 section exports heat from the ocean to the atmosphere year-round. Moreover, the negative trend of  $-2.6 \times 10^{-2}$  PW per decade shown in GLORYS implies that the basin will export heat to the atmosphere in a greater amount each decade.

The freshwater fluxes from hydrography ( $0.6 \pm 0.1$ ,  $0.3 \pm 0.1$  and  $0.6 \pm 0.1$  Sv in 1997, 2003 and 2012, respectively) show that the precipitation and river runoff is higher than the evaporation. When analyzed by monthly means with the GLORYS output, only the spring season shows an evaporation higher than precipitation and runoff. Moreover, the positive trend of  $8.1 \times 10^{-2}$  Sv per decade of the freshwater flux implies that the precipitation and runoff has increased over the evaporation over the decades.

#### Declaration of Competing Interest

The authors declare that they have no known competing financial interests or personal relationships that could have appeared to influence the work reported in this paper.

#### Data availability

Data will be made available on request.

#### Acknowledgments

This work has been completed as part of the doctoral program in Oceanography and Global Change at IOCAG. The first author would like to thank the “Ministerio de Universidades” grant program of “Formación de Profesorado Universitario” for the grant FPU20/02211. V. Caínzos and C. Arumí-Planas acknowledge the Agencia Canaria de Investigación, Innovación y Sociedad de la Información (ACIISI) grant program of “Apoyo al personal investigador en formación” TESIS2019010015 and TESIS2021010028, respectively. This study was supported by the SAGA project (RTI2018-100844-B-C31) funded by the Ministerio de Ciencia, Innovación y Universidades of the Spanish Government. This article is a publication of the Unidad Océano y Clima from Universidad de Las Palmas de Gran Canaria, an R&D&I CSIC-associate unit. This study has been performed as part of the World Ocean Circulation Experiment (WOCE-WHP) project and the Climate Variability Hydrographic Program (CLIVAR) project funded by the National Science Foundation. We gratefully acknowledge the major efforts of the chief scientists that collected these transect data: R. Pickart, J. Toole, A. MacDonald and M. McCartney. The authors declare no competing interests. Finally, the authors gratefully acknowledge M. Cubas-Armas for her help with the data analysis and representation.

#### Data Availability Statement.

The cruise reports, details of the measurements and the hydrographic data can be found at the CLIVAR and Carbon Hydrographic Data Office (CCHDO) webpage (<https://cchdo.ucsd.edu/>). LADCP data sets were acquired from the Global Ocean Ship-based Hydrographic Investigations Program LADCP’s archive (<http://currents.soest.hawaii.edu/clivar/ladcp>). The wind data were collected from the National Center for

Environmental Prediction Reanalysis II (NCEP-DOE) project from the National Oceanic and Atmospheric Administration (NOAA; <https://psl.noaa.gov/data/gridded/data.ncep.reanalysis2.html>). ECCO data are available for download at <https://ecco.jpl.nasa.gov/>. MOM data are available at <https://www.gfdl.noaa.gov/mom-ocean-model/>. GLORYS data are available for download at <https://resources.marine.copernicus.eu/>.

## References

- Adcroft, A., Anderson, W., Balaji, V., Blanton, C., Bushuk, M., Dufour, C.O., Dunne, J.P., Griffies, S.M., Hallberg, R., Harrison, M.J., Held, I.M., Jansen, M.F., John, J.G., Krasting, J.P., Langenhorst, A.R., Legg, S., Liang, Z., McHugh, C., Radhakrishnan, A., Reichl, B.G., Rosati, T., Samuels, B.L., Shao, A., Stouffer, R., Winton, M., Wittenberg, A.T., Xiang, B., Zadeh, N., Zhang, R., 2019. The GFDL Global ocean and sea ice model OM4.0: model description and simulation features. *J. Adv. Model Earth Syst.* 11, 3167–3211. <https://doi.org/10.1029/2019MS001726>.
- Alexander-Astiz Le Bras, I., Sonnewald, M., Toole, J.M., 2019. A barotropic vorticity budget for the subtropical North Atlantic Based on Observations. *J. Phys. Oceanogr.* 49, 2781–2797. <https://doi.org/10.1175/JPO-D-19-0111.1>.
- Bower, A., Lozier, S., Biastoch, A., Drouin, K., Foukal, N., Furey, H., Lankhorst, M., Rühls, S., Zou, S., 2019. Lagrangian views of the pathways of the Atlantic Meridional Overturning Circulation. *J. Geophys. Res. Oceans* 124, 5313–5335. <https://doi.org/10.1029/2019JC015014>.
- Bryden, H.L., Johns, W.E., Saunders, P.M., 2005. Deep western boundary current east of Abaco: Mean structure and transport. *J. Mar. Res.* 63, 35–57. <https://doi.org/10.1357/0022240053693806>.
- Casanova-Masjoan, M., Pérez-Hernández, M.D., Pickart, R.S., Valdimarsson, H., Ólafsdóttir, S.R., Macrandrer, A., Grisolia-Santos, D., Torres, D.J., Jónsson, S., Våge, K., Lin, P., Hernández-Guerra, A., 2020. Along-Stream, Seasonal, and Interannual Variability of the North Icelandic Irmingier Current and East Icelandic Current Around Iceland. *J. Geophys. Res. Oceans* 125, e2020JC016283. <https://doi.org/10.1029/2020JC016283>.
- Casanova-Masjoan, M., Joyce, T.M., Pérez-Hernández, M.D., Vélez-Belchí, P., Hernández-Guerra, A., 2018. Changes across 66°W, the Caribbean Sea and the Western boundaries of the North Atlantic Subtropical Gyre. *Prog. Oceanogr.* 168, 296–309. <https://doi.org/10.1016/j.pocan.2018.09.013>.
- Comas-Rodríguez, I., Hernández-Guerra, A., McDonagh, E.L., 2010. Referencing geostrophic velocities using ADCP data. *Sci Mar* 74, 331–338. <https://doi.org/10.3989/scimar.2010.74n2331>.
- Forget, G., Campin, J.-M., Heimbach, P., Hill, C.N., Ponte, R.M., Wunsch, C., 2015. ECCO version 4: an integrated framework for non-linear inverse modeling and global ocean state estimation. *Geosci Model Dev* 8, 3071–3104. <https://doi.org/10.5194/gmd-8-3071-2015>.
- Fukumori, I., Wang, O., Fenty, I., Forget, G., Heimbach, P., Ponte, R.M., 2021. Synopsis of the ECCO Central Production Global Ocean and Sea-Ice State Estimate, Version 4 Release 4. <https://doi.org/10.5281/ZENODO.4533349>.
- Garzoli, S.L., 2004. North Brazil Current retroflection and transports. *J. Geophys. Res.* 109, C01013. <https://doi.org/10.1029/2003JC001775>.
- Hall, M.M., 2004. Zonal circulation across 52°W in the North Atlantic. *J. Geophys. Res.* 109, C11008. <https://doi.org/10.1029/2003JC002103>.
- Hellerman, S., 1980. Charts of the variability of the wind stress over the tropical Atlantic, in: *Oceanography and Surface Layer Meteorology in the B/C Scale*. Elsevier, pp. 63–75. <https://doi.org/10.1016/B978-1-4832-8366-1.50022-4>.
- Hernández-Guerra, A., Machin, F., Antoranz, A., Cisneros-Aguirre, J., Gordo, C., Marrero-Díaz, A., Martínez, A., Ratsimandresy, A.W., Rodríguez-Santana, A., Sangrá, P., López-Laázen, F., Parrilla, G., Pelegrí, J.L., 2002. Temporal variability of mass transport in the Canary Current. *Deep Sea Research Part II: Topical Studies in Oceanography* 49, 3415–3426. [https://doi.org/10.1016/S0967-0645\(02\)00092-9](https://doi.org/10.1016/S0967-0645(02)00092-9).
- Hernández-Guerra, A., Joyce, T.M., Fraile-Nuez, E., Vélez-Belchí, P., 2010. Using Argo data to investigate the Meridional Overturning Circulation in the North Atlantic. *Deep Sea Res. Part I* 57, 29–36. <https://doi.org/10.1016/j.dsr.2009.10.003>.
- Jackett, D.R., McDougall, T.J., 1997. A Neutral Density Variable for the World's Oceans. *J. Phys. Oceanogr.* 27, 237–263. [https://doi.org/10.1175/1520-0485\(1997\)027<0237:ANDVFT>2.0.CO;2](https://doi.org/10.1175/1520-0485(1997)027<0237:ANDVFT>2.0.CO;2).
- Johns, W.E., Beal, L.M., Baringer, M.O., Molina, J.R., Cunningham, S.A., Kanzow, T., Rayner, D., 2008. Variability of Shallow and Deep Western Boundary Currents off the Bahamas during 2004–05: Results from the 26°N RAPID-MOC Array. *J. Phys. Oceanogr.* 38, 605–623. <https://doi.org/10.1175/2007JPO3791.1>.
- Joyce, T.M., Hernandez-Guerra, A., Smethie, W.M., 2001. Zonal circulation in the NW Atlantic and Caribbean from a meridional World Ocean Circulation Experiment hydrographic section at 66°W. *J. Geophys. Res. Oceans* 106, 22095–22113. <https://doi.org/10.1029/2000JC000268>.
- Joyce, T.M., Thomas, L.N., Dewar, W.K., Girton, J.B., 2013. Eighteen Degree Water formation within the Gulf Stream during CLIMODE. *Deep Sea Res* 2 Top Stud Oceanogr 91, 1–10. <https://doi.org/10.1016/j.dsr2.2013.02.019>.
- Kanamitsu, M., Ebisuzaki, W., Woollen, J., Yang, S.-K., Hnilo, J.J., Fiorino, M., Potter, G. L., 2002. NCEP-DOE AMIP-II Reanalysis (R-2). *Bull Am Meteorol Soc* 83, 1631–1644. <https://doi.org/10.1175/BAMS-83-11-1631>.
- Lee, T., Cornillon, P., 1995. Temporal variation of meandering intensity and domain-wide lateral oscillations of the Gulf Stream. *J. Geophys. Res.* 100, 13603. <https://doi.org/10.1029/95JC01219>.
- Lellouche, J.-M., Greiner, E., le Galloudec, O., Garric, G., Regnier, C., Drevillon, M., Benkiran, M., Testut, C.-E., Bourdalle-Badie, R., Gasparin, F., Hernandez, O., Levrier, B., Drillet, Y., Remy, E., le Traon, P.-Y., 2018. Recent updates to the Copernicus Marine Service global ocean monitoring and forecasting real-time 1/12° high-resolution system. *Ocean Sci.* 14, 1093–1126. <https://doi.org/10.5194/os-14-1093-2018>.
- Meinen, C.S., Garzoli, S.L., 2014. Attribution of Deep Western Boundary Current variability at 26.5°N. *Deep Sea Res. Part I* 90, 81–90. <https://doi.org/10.1016/j.dsr.2014.04.016>.
- Munk, W.H., 1950. On The Wind-driven Ocean Circulation. *J. Meteorol.* 7, 80–93. [https://doi.org/10.1175/1520-0469\(1950\)007<0080:OTWDOC>2.0.CO;2](https://doi.org/10.1175/1520-0469(1950)007<0080:OTWDOC>2.0.CO;2).
- Pérez-Hernández, M.D., Hernández-Guerra, A., Fraile-Nuez, E., Comas-Rodríguez, I., Benítez-Barrios, V.M., Domínguez-Yanes, J.F., Vélez-Belchí, P., de Armas, D., 2013. The source of the Canary current in fall 2009. *J. Geophys. Res. Oceans* 118, 2874–2891. <https://doi.org/10.1002/jgrc.20227>.
- Pérez-Hernández, M.D., Joyce, T.M., 2014. Two Modes of Gulf Stream Variability Revealed in the Last Two Decades of Satellite Altimeter Data. *J. Phys. Oceanogr.* 44, 149–163. <https://doi.org/10.1175/JPO-D-13-0136.1>.
- Pérez-Hernández, M.D., Pickart, R.S., Torres, D.J., Bahr, F., Sundfjord, A., Ingvaldsen, R., Renner, A.H.H., Beszczynska-Möller, A., Appen, W., Pavlov, V., 2019. Structure, Transport, and Seasonality of the Atlantic Water Boundary Current North of Svalbard: Results From a Yearlong Mooring Array. *J. Geophys. Res. Oceans* 124, 1679–1698. <https://doi.org/10.1029/2018JC014759>.
- Rayner, D., Hirschi, J.-J.-M., Kanzow, T., Johns, W.E., Wright, P.G., Frajka-Williams, E., Bryden, H.L., Meinen, C.S., Baringer, M.O., Marotzke, J., Beal, L.M., Cunningham, S. A., 2011. Monitoring the Atlantic meridional overturning circulation. *Deep Sea Res. Part II* 58, 1744–1753. <https://doi.org/10.1016/j.dsr2.2010.10.056>.
- Reid, J.L., 1994. On the total geostrophic circulation of the North Atlantic Ocean: Flow patterns, tracers, and transports. *Prog Oceanogr* 33, 1–92. [https://doi.org/10.1016/0079-6611\(94\)90014-0](https://doi.org/10.1016/0079-6611(94)90014-0).
- Sato, O.T., Rossby, T., 1995. Seasonal and low frequency variations in dynamic height anomaly and transport of the Gulf Stream. *Deep Sea Research Part I: Oceanographic Research Papers* 42 (1), 149–164. [https://doi.org/10.1016/0967-0637\(94\)00034-P](https://doi.org/10.1016/0967-0637(94)00034-P). ISSN 0967-0637.
- Schott, F.A., Zantopp, R., Stramma, L., Dengler, M., Jü, J., Fischer, J., Wibaux, M., 2004. Circulation and Deep-Water Export at the Western Exit of the Subpolar North Atlantic. *J. Phys. Oceanogr.* 34, 817–843. [https://doi.org/10.1175/1520-0485\(2004\)034](https://doi.org/10.1175/1520-0485(2004)034).
- Stewart, K.D., Kim, W.M., Urakawa, S., Hogg, A.M., Yeager, S., Tsujino, H., Nakano, H., Kiss, A.E., Danabasoglu, G., 2020. JRA55-do-based repeat year forcing datasets for driving ocean-sea-ice models. *Ocean Model (Oxf)* 147, 101557. <https://doi.org/10.1016/j.ocemod.2019.101557>.
- Stommel, H., 1948. The westward intensification of wind-driven ocean currents. *Trans. Am. Geophys. Union* 29, 202. <https://doi.org/10.1029/TR029i002p00202>.
- Stommel, H., Arons, A.B., Faller, A.J., 1958. Some Examples of Stationary Planetary Flow Patterns in Bounded Basins. *Tellus* 10, 179–187. <https://doi.org/10.3402/tellusa.v10i2.9238>.
- Stramma, L., 1984. Geostrophic transport in the Warm Water Sphere of the eastern subtropical North Atlantic. *J. Mar. Res.* 42, 537–558. <https://doi.org/10.1357/00222408478856022>.
- Toole, J.M., Curry, R.G., Joyce, T.M., McCartney, M., Peña-Molino, B., 2011. Transport of the North Atlantic Deep Western Boundary Current about 39°N, 70°W: 2004–2008. *Deep Sea Res. Part II* 58, 1768–1780. <https://doi.org/10.1016/j.dsr2.2010.10.058>.
- Toole, J.M., Andres, M., le Bras, I.A., Joyce, T.M., McCartney, M.S., 2017. Moored observations of the Deep Western Boundary Current in the NW Atlantic: 2004–2014. *J. Geophys. Res. Oceans* 122, 7488–7505. <https://doi.org/10.1002/2017JC012984>.
- Tracey, K.L., Watts, D.R., 1986. On Gulf Stream meander characteristics near Cape Hatteras. *J. Geophys. Res.* 91, 7587. <https://doi.org/10.1029/JC091iC06p07587>.
- Tsujino, H., Urakawa, L.S., Griffies, S.M., Danabasoglu, G., Adcroft, A.J., Amaral, A.E., Arsouze, T., Bentsen, M., Bernardello, R., Böning, C.W., Bozec, A., Chassignet, E.P., Danilov, S., Dussins, R., Exarchou, E., Fogli, P.G., Fox-Kemper, B., Guo, C., Ilıcak, M., Iovino, D., Kim, W.M., Koldunov, N., Lapin, V., Li, Y., Lin, P., Lindsay, K., Liu, H., Long, M.C., Komuro, Y., Marsland, S.J., Masina, S., Nummelin, A., Rieck, J.K., Ruppich-Robert, Y., Scheinert, M., Sicardi, V., Sidorenko, D., Suzuki, T., Tatebe, H., Wang, Q., Yeager, S.G., Yu, Z., 2020. Evaluation of global ocean-sea-ice model simulations based on the experimental protocols of the Ocean Model Intercomparison Project phase 2 (OMIP-2). *Geosci Model Dev* 13, 3643–3708. <https://doi.org/10.5194/gmd-13-3643-2020>.
- Våge, K., Pickart, R.S., Spall, M.A., Moore, G.W.K., Valdimarsson, H., Torres, D.J., Erofeeva, S.Y., Nilsen, J.E.Ø., 2013. Revised circulation scheme north of the Denmark Strait. *Deep Sea Res. Part I* 79, 20–39. <https://doi.org/10.1016/j.dsr.2013.05.007>.
- Vélez-Belchí, P., Pérez-Hernández, M.D., Casanova-Masjoan, M., Cana, L., Hernández-Guerra, A., 2017. On the seasonal variability of the Canary Current and the Atlantic Meridional Overturning Circulation. *J. Geophys. Res. Oceans* 122, 4518–4538. <https://doi.org/10.1002/2017JC012774>.
- Worthington, L. v., 1976. On the North Atlantic circulation.
- Wunsch, C., 1978. The North Atlantic general circulation west of 50°W determined by inverse methods. *Rev. Geophys.* 16, 583–620. <https://doi.org/10.1029/RG016i004p00583>.
- Wunsch, C., 1996. The Steady Ocean Circulation Inverse Problem, in: *The Ocean Circulation Inverse Problem*. Cambridge University Press, pp. 212–296. <https://doi.org/10.1017/CBO9780511629570.006>.